Nanoscale

Volume 1 | Number 1 | Jan 2013 | Pages 1–100

Nanoscale

www.rsc.org/nanoscale

ROYAL SOCIETY
OF CHEMISTRY

ROYAL SOCIETY
OF CHEMISTRY

www.rsc.org/nanoscale

Journal Name

Nanoscale

ARTICLE TYPE

Growth and composition of nanostructured and nanoporous cerium oxide thin films on graphite foil

Jaroslava Lavkova,*[a,b] Ivan Khalakhan[a], Mykhailo Chundak[a], Mykhailo Vorokhta[a], Valerie Potin[b], Vladimir Matolin[a], Iva Matolinova[a]

Morphology and composition of CeO_x films prepared by r.f. magnetron sputtering on a graphite foil have been investigated mainly by using microscopy tools. This study has presented formation of nanocrystalline layers with porous structure due to the modification of carbon support and formation of cerium carbide crystallites as a result of the deposition process. Chemical analyses of the layers with 10 different thicknesses performed by energy dispersive X-ray spectroscopy, electron energy loss spectroscopy and X-ray photoelectron spectroscopy have pointed out to the reduction of the cerium oxide layers. In the deposited layers, cerium was present in mixed Ce^{3+} and Ce^{4+} valence. Ce^{3+} species were located mainly at the graphite foil–CeO_x interface and the chemical state of cerium was gradually changing to Ce^{4+} going to the layer surface. It became more stoichiometric in case of thicker layers except of the surface region, where presence of Ce^{3+} was associated with oxygen vacancies on the surface of cerium oxide grains. Degree of the cerium oxide reduction is 15 discussed in the context of particle size.

Introduction

Recently, the claim for renewable energy sources has increased significantly due to spreading of portable electronic 20 devices. To satisfy this claim, a high-density power source has come in need, for example, micro-fuel cell devices (μ-FC). As fuel cell efficiency is higher at smaller scales, μ-FC may have an ideal potential to replace existing batteries whose energy capabilities are limited by the amount of stored chemicals. 25 However, the device cost is still a big limitation, because all devices require an efficient catalyst material, which is usually platinum. To reduce the cost of a fuel cell device, an option is to replace platinum by cheaper material with similar catalytic properties, as Pt has. One of the very promising materials is 30 CeO_x, which has recently been gaining a lot of researchers' attention [1-13]. Cerium oxide is valued for its high oxygen storage capacity, i.e. ability to easily release, store or transport oxygen accompanied by transition between two stable states [14, 15], Ce^{3+} and Ce^{4+}, and for its ability to enhance the activity of transient 35 metal and metal oxide catalysts [15-24].

Very recently, nanostructured $Pt-CeO_x$ material suitable as anode catalyst for proton exchange membrane fuel cells (PEMFC) was reported [25-28]. It is based on ionic Pt^{n+}- doped cerium oxide layers prepared by simultaneous magnetron 40 sputtering of Pt and CeO_2, which exhibits an exceptionally high specific power at a substantial reduction of platinum amount usually used in fuel cells. High activity of the catalyst $Pt-CeO_x$ is related to atomically dispersed platinum on the surface of nanostructured ceria. It is stabilized in the form of a Pt^{2+} ion 45 placed inside a square O_4 nanopocket at {100} nanofacets of CeO_2 [29].

In addition to high efficiency of the catalyst material, it is also necessary to ensure the highest specific surface area of the catalyst. The size, structure and morphology of the catalyst 50 surface depend mainly on the method and parameters of its preparation, as well as on the chosen substrate. Carbon has been proven to be suitable catalyst carrier. Due to superior electrical and physical properties [30-32], carbon materials are of interest for developing modified nanostructured surfaces with high specific 55 area, for example by plasma treatment [33-35]. Moreover, carbon is commonly used material in PEMFC in the form of microfibers of a gas diffusion layer (GDL).

In our previous studies, we presented a simple elaboration technique based on r.f. magnetron sputtering. The method 60 suitable for commercial purposes for mass production is able to fabricate nanoporous and nanostructured CeO_x materials on carbon substrates. The prepared layers have exhibited a complex porous columnar structure with an increased active surface of the catalyst compared to a relatively flat layer deposited on a silicon 65 substrate [25, 26, 28, 36-39]. In very recent works [40, 41], we have shown that morphology of the nanostructured ceria layers can be tuned by different preparation conditions, mainly by working gas composition, r.f. discharge power and deposition time.

In this study, we report structural and chemical 70 characterization of cerium oxide thin layers sputtered on a graphite foil (C-foil) by using atomic force microscopy (AFM), scanning electron microscopy (SEM), transmission electron microscopy (TEM), energy dispersive X-ray spectroscopy (EDX), electron energy loss spectroscopy (EELS) and X-ray 75 photoelectron spectroscopy (XPS) techniques. Morphology observations, crystallographic structures determination and chemical analyses of cerium oxidation states have been performed for different thicknesses of deposited CeO_x layers. Obtained results have pointed to a crucial role of the carbon

substrate in formation of the highly porous nanostructured CeO_x layers (in that case Pt-non-doped ones for simplicity). Moreover, local variations in the Ce ion valences have been shown.

Experimental details

5 The commercial graphite foil (Alfa Aesar, purity 99.8% thickness 0.254 mm) was used as a catalyst substrate. Non-doped ceria thin films were deposited by the r.f. magnetron sputtering. Deposition was carried out at room temperature in argon atmosphere at total pressure of $4x10^{-1}$ Pa. The CeO_2 sputtering 10 was performed perpendicularly to the C-foil surface by using 2-inch CeO_2 target at distance of 90 mm from the substrates with r.f. power of 100 W and an average deposition rate of 1 nm.min^{-1}. The deposition rate was determined from cerium oxide deposition time and ceria layers thickness sputtered on a silicon substrate as 15 a reference during the same deposition process.

Designation of the prepared samples as well as the amount of deposited cerium oxide on the carbon substrate is based on measured thickness of cerium oxide layers prepared simultaneously on the silicon substrate due to their compact 20 character [25, 28]. Thus it is appreciated that these thickness (hereinafter labeled as nominal thickness) values differ from the real thicknesses of the catalyst layers on the C-foil.

Characterizations of all cerium oxide layer samples were performed ex-situ. Surface roughness and thickness 25 measurements of the prepared samples were done using a Veeco di MultiMode V atomic force microscope in tapping mode. Sharpened silicon probes (RFESP, Veeco) with nominal tip radius of curvature 8–10 nm were used in the AFM.

Morphology of prepared cerium oxide thin films was 30 examined by means of scanning electron microscopy using a MIRA Tescan microscope with 30 kV applied voltage for electron beam.

Cross-sectional samples in a form of lamella for transmission electron microscopy observations were prepared using a focused 35 ion beam (FIB) in a LYRA Tescan dual beam microscope equipped with a gas injection system (GIS) by traditional lift-out method [42, 43]. Platinum or silicon oxide was used as a protection layer. The final two-step polishing of the lamellas was performed with gallium ion beam energies of 30 keV at first and of 10 keV 40 afterwards to minimize amorphization of the layers. Average thickness of the lamellas was about 60 nm.

TEM observations were performed using JEOL 2100 FEG microscope, with 200 kV acceleration voltage. Crystal structure of the prepared cross-sectional samples was studied by TEM in 45 high resolution (HRTEM) and scanning (STEM) modes. The experimentally observed crystallographic structures were compared with simulations obtained by Java Electron Microscopy Software [44].

Chemical characterizations in TEM were carried out by means 50 of energy dispersive X-rays spectroscopy (EDX) and electron energy loss spectroscopy (EELS). The EELS spectra of the Ce M_{4-5} edges were acquired with a 1.5 nm probe, an energy dispersion of 0.3 eV/per channel and a Gatan Imaging Filter aperture of 2 nm. EELS linescans were obtained in STEM mode 55 from the C-foil – CeO_x interface to the surface of the 5 nm CeO_x layer with short acquisition times (1 s) in order to minimize electron-beam damage of the sample. The ratio of integrated areas of M_5 and M_4 cerium peaks (A_{M5}/A_{M4}) was determined from the measured EELS spectra applying the second derivative 60 method [45] after background subtraction using the Digital Micrograph software [46].

Chemical states of prepared ceria layers were investigated by means of X-ray photoelectron spectroscopy (XPS) in an ultra-high vacuum system with a base pressure of $2x10^{-8}$ Pa equipped 65 with a SPECS Phoibos MCD 9 hemispherical electron energy analyzer and a dual Mg/Al K_α X-ray source. XPS spectra of Ce 3d, C 1s and O 1s core levels were acquired at normal photoelectron emission geometry using photon excitation energy of hv = 1486.6 eV (Al K_α) with total energy resolution 70 $\Delta E = 1$ eV. Deconvolution of Ce 3d spectra was carried out using the procedure employed by Skala et al. [47]

Results and Discussion

In order to study catalyst-support interaction and fundamental processes resulting in the highly porous structure of cerium oxide 75 on carbon substrates, C-foil substrates were exposed to the cerium oxide sputtering for several different periods of time. In such a way series of cerium oxide layers with different thicknesses were prepared. Fig. 1 presents SEM top-view images of as-prepared films from which is evident an evolution of 80 morphology and surface porosity of the layers with the increasing amount of deposited cerium oxide. At an early stage of growth (the nominal layers thicknesses of 0.5 nm and 1 nm) individual nuclei are formed and a grainy structure starts to be seen on the C-foil surface. With the thicker layers of cerium oxide (nominal 85 thicknesses in the range of 1.5-5 nm) the grains grow and merge to form fractal-like nature of the surface. With further increase in the thickness of the layers (12 nm and 20 nm) the SEM micrographs clearly show columnar character of the prepared layers. For 30 nm deposited cerium oxide, the catalyst layer on 90 the C-foil becomes more compact. The same character of the cerium oxide growth was observed in our previous works on other carbonaceous substrates like CNTs [25], glassy carbon [39], sputtered layers of amorphous carbon [41] and nitrogenized amorphous carbon [40].

95 The three samples with the nominal thicknesses of the catalyst layer of 1 nm, 5 nm and 20 nm (marked CeO_x (1 nm)/C-foil, CeO_x (5 nm)/C-foil, CeO_x (20 nm)/C-foil, respectively) were chosen to take shape of a thin lamella suitable for TEM observation. The micrographs of the side-view of the layers 100 obtained by TEM in scanning mode (STEM) are presented in Fig. 2. A difference in the surface morphology is clearly seen. For 1 nm of cerium oxide deposited on the C-foil (Fig. 2a) the carbon surface remains relatively smooth. The layer roughness determined on the base of AFM measurement is about 3-4 nm 105 and corresponds very well to HRTEM observations (see Fig. 3a). In case of 5 nm thick catalyst layer (Fig. 2b), STEM image displays considerable increase of the surface roughness. Moreover, from the material contrast, one can see that hilly-like structure is created by carbon substrate, while cerium oxide just 110 copies the formed shapes. The relative height of the structure is around 30 nm. For the sample with 20 nm of deposited cerium oxide, the formed porous structure is estimated to be 90 - 100 nm tall (Fig. 2c). So it is 5 times more than the thickness of the deposited catalyst layer measured on the reference silicon

substrate, wherein the layer grows compact [25], [28]. These observations and results suggest that carbon substrate plays an active role supporting the porosity of the catalyst layer during the growth.

With purpose to verify chemical composition of the columnar structures created during the deposition of the 20 nm thick cerium oxide layer on the C-foil, EDX measurements of the cross-sectional sample in a form of thin lamella were carried out. The superposed EDX maps of C, Ce and Pt elements displayed in Fig. 2d point to the presence of carbon inside the formed structures with cerium rich layer covering the hilly surface and occurring mostly on the caps. Note that platinum was used as a protection layer during the lamella preparation. Thus EDX element mapping confirms the hypothesis made on the basis of material contrast of the STEM images in the Fig. 2b and c.

The crystallographic studies of the three samples (nominal thicknesses of CeO_x layers 1, 5 and 20 nm, supported by the C-foil) performed by HRTEM point at nanocrystalline character of the sputtered layers. The deposited cerium oxide films are composed of crystallites up to several nanometers in size. The nanoparticles were found to be very small (up to 3 nm in diameter) inside the carbon pores and reached bigger size (up to 10 nm) on top of the caps when sufficient amount of CeO_2 was deposited. Regardless of quantity of deposited cerium oxide and roughness of carbon-cerium oxide interfaces, major part of recorded crystallographic zone axes correspond with distances and angles to CeO_2 [101] and CeO_2 [112] crystals. In Fig. 3a an example of crystallite exhibiting CeO_2 [101] is presented for the CeO_x (1 nm)/C-foil sample, where the deposited layer is non-continuous and individual crystals are observed on the relatively smooth carbon surface. In addition, many crystallites with only measurable interplanar distances were observed, some of them could correspond to Ce_2O_3 crystals. In some cases, recorded zone axes of observed nanocrystals were not in agreement with any zone axis of cerium oxides. It suggested formation of other compounds such as cerium carbides. In accordance with this assumption, several crystallites that can correspond to CeC_2 [111] were detected, see Fig. 3b. Unfortunately, this zone axis has similar distances and angles like CeO_2 [101] or Ce_7O_{12} [310]. Thus, an unambiguous determination of such crystals is not possible within the measurement error. However, we observed several crystals, which could be undeniably indexed as CeC_2 [100], CeC_2 [101] (not shown) and CeC_2 [001] (Fig. 3c). Information gained from HRTEM confirms the formation of cerium carbides during cerium oxide sputtering on the C-foil substrate.

Regarding the localization of nanocrystals (Fig. 3d), cerium carbides were observed mainly near the carbon surface. The places of CeO_2 nanocrystal occurrence were recorded in the deeper areas of the structure and also on the surface of the film, where the size of the nanocrystals was considerably larger.

To verify the roughness of the carbon-cerium oxide interface formed during the sputter deposition, which significantly determines the porosity, the catalyst layer of the CeO_x (5 nm)/C-foil sample was removed off by H_2SO_4 acid. In Fig. 4, images of the sample surfaces are shown before CeO_2 deposition, after it and after removing the deposited cerium oxide layer. Fig. 4a presents the high resolution AFM image of the pure C-foil

composed of atomically smooth graphite sheets where its hexagonal structure is clearly visible. Comparing the images of the CeO_x (5 nm)/C-foil before and after flushing out in the acid obtained by AFM (Figs. 4b and c), SEM (Figs. 4d and e) and TEM (Figs. 4f and g), the similarity in the surface morphology can be seen. The hilly-like character of the structure does not disappear, and the porosity seems to be changed very little. Only the structures look a bit rounder and less pointed, as shown in Figs. 4b and c. Moreover, in the Fig. 4g showing the TEM image of the modified C-foil surface, with the bigger magnification the carbon planes were visible. It confirms that the hilly-like structure is created by carbon. Any crystal containing cerium was not observed inside the structure, neither on the top after washing off the deposited layer. The reason why the surface roughness remained almost unchanged after removal of the catalyst layer is that after deposition, cerium oxide is present on the whole modified surface of carbon; especially atop it has considerably higher amount (see Fig. 2c).

The chemical state and the composition of the catalyst films were investigated by X-ray photoelectron spectroscopy. In Fig. 5a, the Ce 3d core level XPS spectra are compared for the three samples CeO_x (1 nm)/C-foil, CeO_x (5 nm)/C-foil, CeO_x (20 nm)/C-foil, respectively. Each spectrum consists of three $3d_{5/2} - 3d_{3/2}$ spin-orbit-split doublets characteristic for the Ce^{4+} states which are a sign of stoichiometric cerium dioxide (CeO_2) and two doublets evidencing formation of Ce^{3+} ions [48], [49]. An example of the decomposition of the Ce 3d spectrum to sums of Ce^{4+} and Ce^{3+} doublets (according to Skala et al. work [47]) is shown for 1 nm thick layer of CeO_x. From the shapes of the Ce 3d spectra in Fig. 5 one can see that the contribution of the Ce^{3+} states in comparison with Ce^{4+} ones is increasing with the decreasing thickness of the cerium oxide layer. It is necessary to note that XPS represents an integral method of surface science analysis with information depth about 3–5 nm.

In the bottom part of Fig. 5 there are two curves (solid and dotted) added representing Ce 3d spectra taken for the CeO_x (5 nm)/C-foil sample after removal of the catalyst layer in H_2SO_4 acid. Solid line shows the spectrum at the same scale as other Ce 3d spectra are presented. The intensity of the Ce 3d spectra for the sample after flushing out is negligibly small (the bottom solid line). Spectrum multiplied by 10 (the dotted line) shows that cerium is solely in the Ce^{3+} state. The results indicated that it could be the residues of cerium carbide where cerium atoms are in the Ce^{3+} oxidation state [50], [51]. We can conclude that acid treatment successfully removed the ceria layer and only traces of the catalyst can be seen.

An influence of the sputter deposition process of cerium oxide on the C-foil surface is possible to follow in Fig. 5b where core level C 1s spectra are presented for pure graphite foil (the bottom spectrum) and for three CeO_x layers with nominal thicknesses of 1, 5 and 20 nm (three upper spectra). The spectrum of the pure C-foil is asymmetric with main C 1s component centred at 284.5 eV, that can be assigned to the C-C bonding of sp^2 hybridized carbon in the graphitic structure [52], [53]. The non-resolved tail prolonged to higher binding energies indicates that more than one peak contribution is present. With deposition of cerium oxide we found an appearance of a broad shoulder around 288.3 eV in all C 1s spectra acquired on the graphite foil covered with CeO_x layers.

Such a shoulder was observed also in case of the pure graphite sample treated in oxygen plasma for 10 min (dc discharge at current of 1.7 mA and voltage of 430 V in pure oxygen at a total pressure of 20 Pa), see the second curve from bottom in Fig. 5b. The results indicate that presence of the additional peaks in C 1s spectra of the C-foil covered with cerium oxide films is possible directly correlated with a modification of the graphite surface by oxygen plasma. According to the literature, oxygen plasma treatment can lead to increasing the concentration of the oxygen-containing groups on the carbon surface as well as enhancing surface roughness [54]. The peak around 288.3 eV can be related to formation of doubly bonded oxygen to carbon (C=O) [53], but neither contribution of >C=O (carbonyl) and/or –COO groups on the C-foil surface can not be excluded [53, 55-57].

In order to follow changes in oxidation state of cerium in the sputtered CeO_x layers as a function of layer thickness we carried out electron energy loss spectroscopy measurements on the cross-sectional CeO_x (5 nm)/C-foil sample. The EELS spectra of the Ce $M_{4,5}$ edges region were recorded during a linescan made through the catalyst film from the carbon substrate to the layer surface (marked by red arrow in Fig. 2b). An example of two EELS spectra (after subtraction of the background) acquired near the C-foil–CeO_x interface and close to the surface of the deposited cerium oxide layer is presented in Fig. 6a. A shift in energy of more than 1 eV for the Ce M_5 and M_4 maxima peaks positions and an inversion of the M_5 to M_4 intensity ratio can be seen.

As was shown in the literature [58-61], Ce^{3+} $M_{4,5}$ edge shapes, intensities, and energies differ from those of Ce^{4+}. The intensity of the M_4 edge is higher than that of M_5 edge in Ce^{4+} and reversed in Ce^{3+}. For this reason, study of the M_4/M_5 ratio variation is often used to follow local variations in the valence of Ce ions. Typical values of the ratio of integrated areas of M_5 and M_4 cerium peaks (obtained after applying second derivative method), A_{M5}/A_{M4} close to 1.3 and 0.9 are reported for Ce^{3+} and Ce^{4+} states, respectively [58, 59]. For lanthanides the dependency of the ratio on the oxidation state of Ce was found to be linear [59, 61]. Thus, the ratio having a value between 0.9 and 1.3 corresponds to a mix of Ce^{3+} and Ce^{4+}.

In Fig. 6b, the values of A_{M5}/A_{M4} ratio calculated from acquired EELS spectra of the Ce $M_{4,5}$ edges region during the linescan with increasing distance from the C-foil substrate are plotted. The value of the ratio obtained near to the interface with the carbon substrate was almost 1.30 indicating that cerium occurs mostly in reduced state of Ce^{3+}. With moving the probe closely to the layer surface, the ratio is decreasing until the lowest value 1.03. This change in the Ce M_5/M_4 area ratio as well as a chemical shift of the M_5 and M_4 peaks to higher energy indicate that there is a mix of Ce^{3+} and Ce^{4+} states and that from carbon interface to the surface of the catalyst, stoichiometry of ceria is gradually changing from 3+ to 4+. Only at the top of the layer surface, the value of A_{M5}/A_{M4} ratio becomes higher (1.14), which can be associated with oxygen vacancies on the edge of cerium oxide grains forming surface of the deposited layer. The effect of surface reduction on ceria nanoparticles was observed by EELS by several groups [58, 62, 63].

Gilliss et al. have reported in the EELS study [62] that Ce^{3+} is present at the surface of the CeO_2 particles randomly crystallographically orientated and of varying size from tens of nanometers to several hundreds of nanometers. All particles showed similar trends of Ce reduction at the surface, regardless of their size as indicated by the shift of the $M_{4,5}$ to a lower energy and the increase of the M_5/M_4 ratio. High resolution mapping of individual ceria nanoparticles of different sizes [63] confirmed change of the valence of the surface cerium ions from 4+ to 3+ owing to oxygen vacancies close to the surface. The thickness of the reduction shell was found to be dependent upon several parameters such as size of the nanoparticle and a crystallographic type of the ceria surface (on the close-packed {111} surfaces the top layer was found to be fully reduced with the underlying 1-2 atomic layers of mixed valence; at the {100} surface plane, the first 5-6 atomic layers were all in reduced state, intermixing gradually sets in after 5-6 atomic planes). The particle size played a major role; in case of the small nanoparticles (below 5 nm in diameter) EELS showed predominantly Ce^{3+} features (the smallest ones at a size less than 3 nm were fully reduced) even though the nanoparticles retained the fluorite (CeO_2) structure, whilst larger particles appeared to be reduced only in a thin surface shell [58, 63]. For 6 nm and 10 nm size ceria nanoparticles the same effect of the surface reduction accompanied by enhanced Ce^{3+} concentration inside ceria particles was studied using XPS/XANES [64], and complete reduction of ceria particles smaller than 3 nm was confirmed by XPS [65]. In a number of works [58, 66] findings that the fraction of Ce^{3+} ions in the ceria particles rapidly increased with decreasing particle size were accompanied by observations of the lattice parameter expansion. In such cases, changes of lattice parameters of small ceria particles can complicate their crystallographic identification.

To study size dependent reduction of ceria particles, integral methods or techniques with large probe sizes, such as XPS, require a sample with a large assembly of particles unavoidable variations in size or at least very narrow size distribution [65]. This is not the case of nanostructured cerium oxide thin films. Generally, chemical composition, i.e. amount of oxygen, Ce^{3+} and Ce^{4+} contents, of the layers characterized using XPS can be affected by different parameters such as the type of used substrate, the film structure, thickness and morphology. It is dependent on crystal phases and sizes, as well as on layers density, grains size, defects distribution as oxygen vacancies and grain boundaries, and finally on surface and interface roughness. For these reasons, it is very difficult to identify the major affecting factor. In complex study on nanocrystalline CeO_x films mainly consisted of CeO_2 grains [49], considerable concentration of Ce^{3+} was found to be distributed at the CeO_2 grain boundaries forming amorphous Ce_2O_3, whilst only a small portion of Ce^{3+} was located around oxygen vacancy sites.

The above presented results on chemical composition of the sputtered cerium oxide layers supported by the C-foil carried out using XPS (Fig. 5) point to the fact that the catalyst layers are of Ce^{3+} and Ce^{4+} mix valence and the ceria reduction is irreversibly dependent on layer thickness. In the thin CeO_x layers (the nominal thicknesses of 1 nm and 5 nm) cerium occurs substantially in the Ce^{3+} state (43% and 40% of cerium atoms) and with the increasing thickness of the catalyst layer occupies more the Ce^{4+} states. The layer with 20 nm of nominal thickness looks nearly stoichiometric (with 75% of cerium atoms in Ce^{4+}

state). This behavior fits very well with the EELS data obtained by linescan through the 5 nm thick layer from the interface to its surface (Fig. 6). The EELS spectra show reduced cerium oxide at the C-foil–CeO$_x$ layer interface becoming gradually more stoichiometric to the surface. Presence of cerium atoms solely in Ce^{3+} state at the C-foil surface was also confirmed by XPS on the sample after removing the cerium oxide layer in H$_2$SO$_4$ acid.

Knowing the linear dependency of the A$_{M5}$/A$_{M4}$ ratio on the oxidation state of Ce [59, 61] we can estimate a value of the Ce M$_5$/M$_4$ area ratio based on the concentration of Ce^{3+} species determined from XPS Ce 3d spectrum on the CeO$_x$ (5 nm)/C-foil sample. In such a way the 40% of Ce^{3+} species corresponds to the value of 1.06. The value agrees well with the A$_{M5}$/A$_{M4}$ ratios obtained for upper part of the layer (Fig. 6b). It is necessary to note that in case of XPS the Ce^{3+} concentration in a subsurface region is not a simple average value because the signal intensity is attenuated according to the Beer-Lambert law with depth. So, since more reduced cerium oxide occurs at the carbon–CeO$_x$ interface, the Ce^{3+} state is suppressed in this case.

Above presented results allow us to complement the model of the growth of porous cerium oxide layers on carbon substrates proposed in work of Haviar et al. [41] by information on the chemical state of cerium, see Fig. 7. The model is based on dynamic equilibrium between carbon etching and simultaneous deposition of cerium oxide during the process of magnetron sputtering.

The carbon etching process and/or the erosion of carbon substrate surface as a result of reaction of surface carbon atoms with oxygen species present in plasma was confirmed in our previous works [40, 41]. Performed XPS analysis points to an oxidation of the carbon surface during sputter deposition of cerium oxide of similar nature to that which occurs on pure graphite surface treated in oxygen plasma. The C 1s core level spectra (see Fig. 5b) show the presence of oxygen-containing species bounded to carbon on the C-foil surface. According to the literature [67-71], carbon substrate modification by oxygen interaction with carbon atoms and their removal due to the formation of volatile carbon oxides (CO and CO$_2$) can be considered as a universal effect. Paredes et al. [67] reported that chemical reactions between the carbon atoms and the active species from the oxygen plasma constituted the main driving force leading to the formation of defect sites and pits on the large atomically flat terraces of highly oriented pyrolytic graphite. Reactive oxygen species existing in an oxygen plasma cause that surface carbon is gasified resulting in CO and CO$_2$ production. The desorption of CO and CO$_2$ gases removes carbon atoms from solid matrix and etching is occurs [67, 68]. The effect was confirmed by using mass spectroscopy during carbon substrate reactive etching by oxygen plasma [69, 70]. The oxidative etching process on graphite surfaces that forms the CO and CO$_2$ gases was the subject of first principles approach study done by Incze et al. [71].

At early stage of the proposed model describing growth of porous structure of cerium oxide on carbonaceous materials, when only a small amount of cerium oxide is deposited on the surface of a carbon substrate, small nuclei of cerium oxide or other related compounds (e.g. cerium carbides) are formed. It results to fine grainy structure of the deposited layer, observed in Fig. 1 (case of the CeO$_x$ nominal thicknesses of 0.5-1.5 nm), with cerium mainly in Ce^{3+} state. These nuclei and/or small grains are resistant to plasma etching and act as a shielding mask for the underlying carbon substrate. Whilst the uncovered C-foil surface is exposed to plasma during sputter deposition, and carbon etching is the dominating process at this moment. As a consequence, deep hollows are formed under the areas that are not shielded (see Fig. 2). With ongoing deposition of cerium oxide, grains are growing and coalescing (Fig. 1, 1.5–30 nm nominal thicknesses), and cerium oxide becomes more stoichiometric. Thus the non-uniform etching of the C-foil and the deposition of cerium oxide create finally the porous structure of the cerium oxide layer. Cerium has mixed oxidation states varying from Ce^{3+} to Ce^{4+} going through the layer from the carbon–CeO$_x$ interface to the surface as schematically shown in Fig. 7. Cerium is located mainly in the state of Ce^{3+} close to the carbon–layer interface where most of the cerium carbide nanocrystals were observed and in the Ce^{4+} one in atop region of the hilly-like structures, where bigger sized crystallites are located, except at the top layer surface where Ce^{3+} is also present due to oxygen vacancies.

Based on the obtained results, we cannot exclude that the deposited layer contains crystals (although none were clearly identified) or amorphous phase of Ce$_2$O$_3$. Neither we can assess the amount of defects on the surface of the CeO$_2$ nanocrystals or the cerium oxide grains into the layer of nanostructured character. However, it should be borne in mind that the analysis of the oxidation state of cerium into the deposited layers using EELS and XPS spectroscopies has its limitations. The XPS signal is of an integral character over the entire surface of the sample, i.e. XPS "sees" CeO$_x$ of the tops of hilly-like carbon structures as well as on their flanks and across the valley, and a signal from deeper regions of the deposited layers is attenuated. On the other hand, the EELS measurements were done on the cross-sectional sample. During the linescan, the primary beam crossed the hilly-like carbon structures covered by cerium oxide from C-foil–catalyst interface to the top, where intervened only cerium oxide in the form of a cap. So, the EELS signal comes from different places on the CeO$_x$ layer of different thicknesses, and changes in oxidation state of cerium can be locally affected by presence of smaller or bigger CeO$_2$ crystals as discussed above.

Conclusions

In this work the evolution of surface morphology as well as composition of the cerium oxide layers deposited by r.f. magnetron sputtering on the C-foil was shown as a function of the layer thickness. Formation of the nanoporous layers was observed from the early stage of the relatively smooth layer formed from individual nuclei changing through a fractal-like character to the hilly-like structures as the layer thickness was increasing. Roughening of the deposited layers is shown to be connected with roughening of the graphite foil surface due to complex processes occurring during the CeO$_2$ sputtering and/or an interaction between carbon and deposited cerium oxide leading to the C-foil surface erosion and formation of cerium carbides. HRTEM observations confirmed nanocrystalline character of the prepared CeO$_x$ films; CeO$_2$ and CeC$_2$ crystallites of several nanometers in size were identified. Based on the EELS and XPS measurements the layers are partially reduced with

cerium in the mixture of Ce^{3+} and Ce^{4+} oxidation states. The layers were found being fully reduced close to the C-foil–CeO_x interface. The enhanced Ce^{3+} concentration was also observed just at surface region of the prepared CeO_x films associated with oxygen vacancies on the surface of cerium oxide grains. In case of the thicker layers, cerium was gradually varying its valence from 3+ to 4+ going from the carbon–CeO_x interface to the layers surface associated with formation of bigger crystallites in caps atop hilly-like structures. The influence of CeO_2 crystallite size on stoichiometry of the CeO_x layers was discussed.

Acknowledgment

Notes and references

[a] *Department of Surface and Plasma Science, Faculty of Mathematics and Physics, Charles University in Prague, V Holešovičkách 2, 180 00 Prague 8, Czech Republic. Fax: +420 284 685 095; Tel: +420 221 912 733; E-mail: jaroslava.lavkova@gmail.com*
[b] *Laboratoire Interdisciplinaire Carnot de Bourgogne, UMR 6303 CNRS - Université de Bourgogne, 9, avenue Alain Savary, BP 47870, F-21078 Dijon Cedex, France. Fax: +33 380 395 923; Tel: +33 380 395 069; E-mail: jaroslava.lavkova@gmail.com*

1 D. M. Lyons, K. M. Ryan, M. A. Morris, *J. Mater. Chem.*, 2002, **12**, 1207-1212.
2 C.-Y. Cao, Z.-M. Cui, C.-Q. Chen, W.-G. Song, W. Cai, *J. Phys. Chem. C*, 2010, **114**, 9865-9870.
3 J. A. Farmer, C. T. Campbell, *Science*, 2010, **329**, 933-936.
4 T. Yu, J. Zeng, B. Lim, Y. Xia, *Adv. Mater.*, 2010, **22**, 5188–5192.
5 D. Zhang, X. Du, L. Shi, R. Gao, *Dalton Trans.*, 2012, **41**, 14455-14475.
6 C. Slostowski, S. Marre, O. Babot, T. Toupance, C. Aymonier, *Langmuir*, 2014, **30**, 5965-5972.
7 S. Hilaire, L. Luo, F. Rechberger, F. Krumeich, M. Niederberger, *Z. Anorg. Allg. Chem.*, 2014, **640**, 733-737.
8 A. Cyganiuk, R. Klimkiewicz, A. Bumajdad, J. Włoch, A. Kucinska, J. P. Lukaszewicz, *Mater. Lett.*, 2014, **118**, 119-122.
9 I. I. Soykal, H. Sohn, D. Singh, J. T. Miller and U. S. Ozkan, *ACS Catalysis*, 2014, **4**, 585-592.
10 A. Xie, J. Guo, W. Liu, Y. Yang, *RSC Advances*, 2014, **4**, 11357-11359.
11 H. Chen, J. Duan, X. Zhang, Y. Zhang, C. Guo, L. Nie, X. Liu, *Mater. Lett.*, 2014, **126**, 9-12.
12 H.-L. Lin, C.-Y. Wu, R.-K. Chiang, *J. Colloid Interface Sci.*, 2010, **341**, 12-17.
13 B. Puertolas, B. Solsona, S. Agouram, R. Murillo, A. M. Mastral, A. Aranda, S. H. Taylor, T. Garcia, *App. Catal. B*, 2010, **93**, 395-405.
14 N. V. Skorodumova, S.I. Simak, B. I. Lundqvist, I. A. Abrikosov, B. Johansson, *Phys. Rev. Lett.*, 2002, **89**, 166601.
15 J. Kaspar, P. Fornasiero, M. Graziani, *Catal. Today*, 1999, **50**, 285-298.
16 A. Trovarelli, in Catalytic Science Series, ed. G. J. Hutchings, Imperial College Press, London, 2002, vol. 2, ch. 1, pp. 7 - 17.
17 H. Muraki, G. Zhang, *Catal. Today*, 2000, **63**, 337-345.
18 I. D. González, R. M. Navarro, W. Wen, N. Marinkovic, J. A. Rodriguéz, F. Rosa, J. L. G. Fierro, *Catal. Today*, 2010, **149**, 372-379.
19 M. Khajenoori, M. Rezaei, F. Meshkani, *Chem. Eng. Technol.*, 2014, **37**, 957-963.
20 W. Shan, N. Ma, J. Yang, X. Dong, C. Liu, L. Wei, *J. Nat. Gas Chem.*, 2010, **19**, 86-90.
21 X.-N. Wu, Y.-X. Zhao, W. Xue, Z.-C. Wang, S.-G. He, X.-L. Ding, *Phys. Chem. Chem. Phys.*, 20120, **12**, 3984-3997.
22 W. Xu, R. Si, S. D. Senanayake, J. Llorca, H. Idriss, D. Stacchiola, J. C. Hanson, J. A. Rodriguez, *J. Catal.*, 2012, **291**, 117-126.
23 K. Li, H. Wang, Y. Wei, D. Yan, Chem. Eng. J., 2010, 156, 512-518.
24 N. Yi, R. Si, H. Saltsburg, M. Flytzani-Stephanopoulos, *Energy Environ. Sci.*, 2010, **3**, 831-837.
25 V. Matolin, I. Matolinova, M. Vaclavu, I. Khalakhan, M. Vorokhta, R. Fiala, I. Pis, Z. Sofer, J. Poltierova-Vejpravova, T. Mori, V. Potin, H. Yoshikawa, S. Ueda, K. Kobayashi, *Langmuir*, 2010, **26**, 12824-12831.
26 R. Fiala, I. Khalakhan, I. Matolinova, M. Vaclavu, M. Vorokhta, Z. Sofer, S. Huber, V. Potin, V. Matolin, *J. Nanosci. Nanotechnol.*, 2011, **11**, 5062-5067.
27 R. Fiala, M. Vaclavu, A. Rednyk, I. Khalakhan, M. Vorokhta, J. Lavkova, V. Potin, I. Matolinova, V. Matolin, *Catalysis Today*, 2015, **273**, 105-109.
28 V. Matolin, M. Cabala, I. Matolinova, M. Škoda, M. Vaclavu, K.C. Prince, T. Skala, T. Mori, H. Yoshikawa, Y. Yamashita, S. Ueda, K. Kobayashi, *Fuel Cells*, 2010, **10**, 139-144.
29 A. Bruix, Y. Lykhach, I. Matolinova, A. Neitzel, T. Skala, N. Tsud, M. Vorokhta, V. Stetsovych, K. Sevcikova, J. Myslivecek, R. Fiala, M. Vaclavu, K. C. Prince, S. Bruyere, V. Potin, F. Ilias, V. Matolin, J. Libuda, K. M. Neyman, *Angew. Chem. Int. Ed.*, 2014, **53**, 10525–10530.
30 Q. Chen, S. Wang, L.-M. Peng, *Nanotechnology*, 2006, **17**, 1087-1098.
31 H. Dai, E. W. Wong, C. M. Liebert, *Science*, 1996, **272**, 523-526.
32 A. Qureshi, W. P. Kang, J. L. Davison, Y. Gurbuz, *Diamond & Related Materials*, 2009, **18**, 1401-1420.
33 Z. Hou, B. Cai, H. Liu, D. Xu, *Carbon*, 2008, **46**, 405-413.
34 N. M. D. Brown, N. Cui, A. McKinley, *Appl. Surf. Sci.*, 1998, **133**, 157-165.
35 S. I. Stevanovic, V. V. Panic, A. B. Dekanski, A. V. Tripkovic, V. M. Jovanovic, Phys. *Chem. Chem. Phys.*, 2012, **14**, 9475-9485.
36 I. Matolinova, R. Fiala, I. Khalakhan, M. Vorokhta, Z. Sofer, H. Yoshikawa, K. Kobayashi, V. Matolin, *Appl. Surf. Sci.*, 2012, **258**, 2161–2164.
37 V. Matolin, R. Fiala, I. Khalakhan, J. Lavkova, M. Vaclavu, M. Vorokhta, *Int. J. Nanotechnol.*, 2012, **9**, 680-694.
38 M. Vorokhta, I. Khalakhan, I. Matolinova, M. Kobata, H. Yoshikawa, K. Kobayashi, V. Matolin, *Appl. Surf. Sci.*, 2013, **267**, 119-123.
39 I. Khalakhan, M. Dubau, S. Haviar, J. Lavkova, I. Matolinova, V. Potin, M. Vorokhta, V. Matolin, *Ceram. Int.*, 2013, **39**, 3765-3769.
40 M. Dubau, J. Lavkova, I. Khalakhan, S. Haviar, V. Potin, V. Matolin, I. Matolinova, *ACS Appl. Mater. Interfaces*, 2014, **6**, 1213–1218.
41 S. Haviar, M. Dubau, J. Lavkova, I. Khalakhan, V. Potin, V. Matolin, I. Matolinova, *Sci. Adv. Mater.*, 2014, **6**, 1278–1285.
42 L. A. Giannuzzi et al., in *Introduction to Focused Ion Beams*, ed. L. A. Giannuzzi and F. A. Stevie, Springer, Boston, 2005, ch.10, pp. 213-214.
43 R. Wirth, *Chemical Geology*, 2009, **261**, 217-229.
44 P. A. Stadelmann, *Ultramicroscopy*, 1987, **21**, 131-145.
45 G. A. Botton, C. C. Appel, A. Horsewell, W. M. Stobbs, *J. Microsc.*, 1995, **180**, 211–216.
46 Gatan Inc., Digital Micrograph, http://www.gatan.com (accessed September 2014).
47 T. Skala, F. Sutara, K. C. Prince, V. Matolin, *J. Electron Spectrosc. Relat. Phenom.*, 2009, **169**, 20-25.
48 M. Romeo, K. Bak, J. El Fallah, F. Le Normand and L. Hilaire, *Surf. Interface Anal.*, 1993, **20**, 508-512.
49 P. Patsalas, S. Logothetidis, L. Sygellou, S. Kennou, *Phys. Rev. B*, 2003, **68**, 035104.
50 M. Atoji, *The Journal of Chemical Physics*, 1967, **46**, 1891-1901.
51 T. Sakai, G. Adachi, T. Yoshida, J. Shiokawa, *J. Chem. Phys.*, 1981, **75**, 3027-3032.
52 J. L. Figueiredo, M. F. R. Pereira, *Catalysis Today*, 2010, **150**, 2-7.

53 A. Ganguly, S. Sharma, P. Papakonstantinou, J. Hamilton, *J. Phys. Chem. C*, 2011, **115**, 17009-17019.

54 W. Li, S. Y. Yao, K. M. Ma, P. Chen, *Polymer Composites*, 2013, **34**, 368-375.

5 55 T.I.T. Okpalugo, P. Papakonstantinou, H. Murphy, J. McLaughlin, N.M.D. Brown, *Carbon*, 2005, **43**, 153-161.

56 Y.-Q. Wang, F.-Q. Zhang, P. M. A. Sherwood, *Chem. Mater.*, 1999, **11**, 2573-2583.

57 D. Yang, A. Velamakanni, G. Bozoklu, S. Park, M. Stoller, R.D. Piner, 10 S. Stankovich, I. Jung, D. A. Field, C. A. Ventrice Jr., R. S. Ruoff, *Carbon*, 2009, **47**, 145-152.

58 L. Wu, H. J. Wiesmann, A. R. Moodenbaugh, R. F. Klie, Y. Zhu, D. O. Welch, M. Suenaga, *Phys. Rev. B*, 2004, **69**, 125415.

59 G. Yang, G. Möbus, R. J. Hand, *Micron*, 2006, **37**, 433-441.

15 60 L. A. J. Garvie, P. R. Buseck, J. Phys. *Chem. Solids*, 1999, **60**, 1943-1947.

61 H. Xu, Y. Wang, J. Nucl. Mat., 1999, 266, 117-123.

62 S. R. Gilliss, J. Bentley, C. B. Carter, *App. Surf. Sci.*, 2005, **241**, 61–67.

20 63 S. Turner, S. Lazar, B. Freitag, R. Egoavil, J. Verbeeck, S. Put, Y. Strauven, G. Van Tendeloo, *Nanoscale*, 2011, **3**, 3385.

64 F. Zhang, P. Wang, J. Koberstein, S. Khalid, S.-W. Chan, *Surf. Sci.*, 2004, **563**, 74-82.

65 S. Tsunekawa, T. Fukuda, A. Kasuya, *Surf. Sci.*, 2000, **457**, L437-25 L440.

66 S. Tsunekawa, R. Sahara, Y. Kawazoe, K. Ishikawa, *Appl. Surf. Sci.*, 1999, **125**, 53-56.

67 J. I. Paredes, A. Martínez-Alonzo, J. M. D. Tascón, *Carbon*, 2000, **38,**, 1183-1197.

30 68 V. G. Zavodinskii, E. A. Mikhailenko, *Combustion, Explosion, and Shock Waves,*,2006, **42**, 247-253.

69 M. A. Baker, *Thin solid films*, 1980*,* **69**, 359–368.

70 V. Philipps, G. Sergienko, A. Lyssoivan, H. G. Esser, M. Freisinger, A. Kreter, U. Samm, *J. Nucl. Mater.*, 2007, **363**, 929–932.

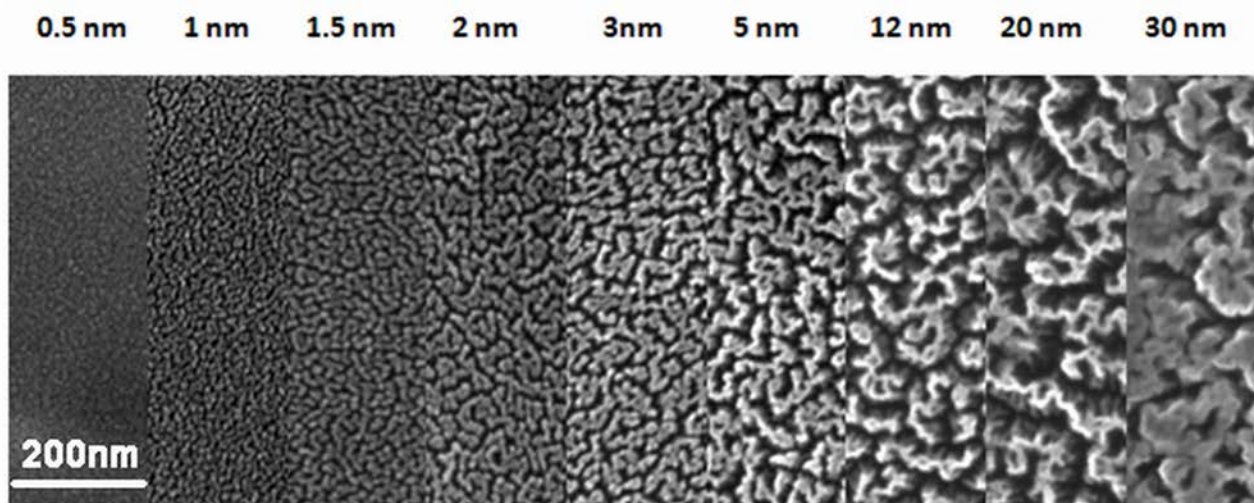35 71 A. Incze, A. Pasturel, C. Chatillon, *Surf. Sci.*, 2003, **537**, 55-63.

Figures

Fig. 1. SEM images of the evolution of surface porosity and morphology of CeO$_x$ on the C-foil substrate as a function of layer nominal thickness.
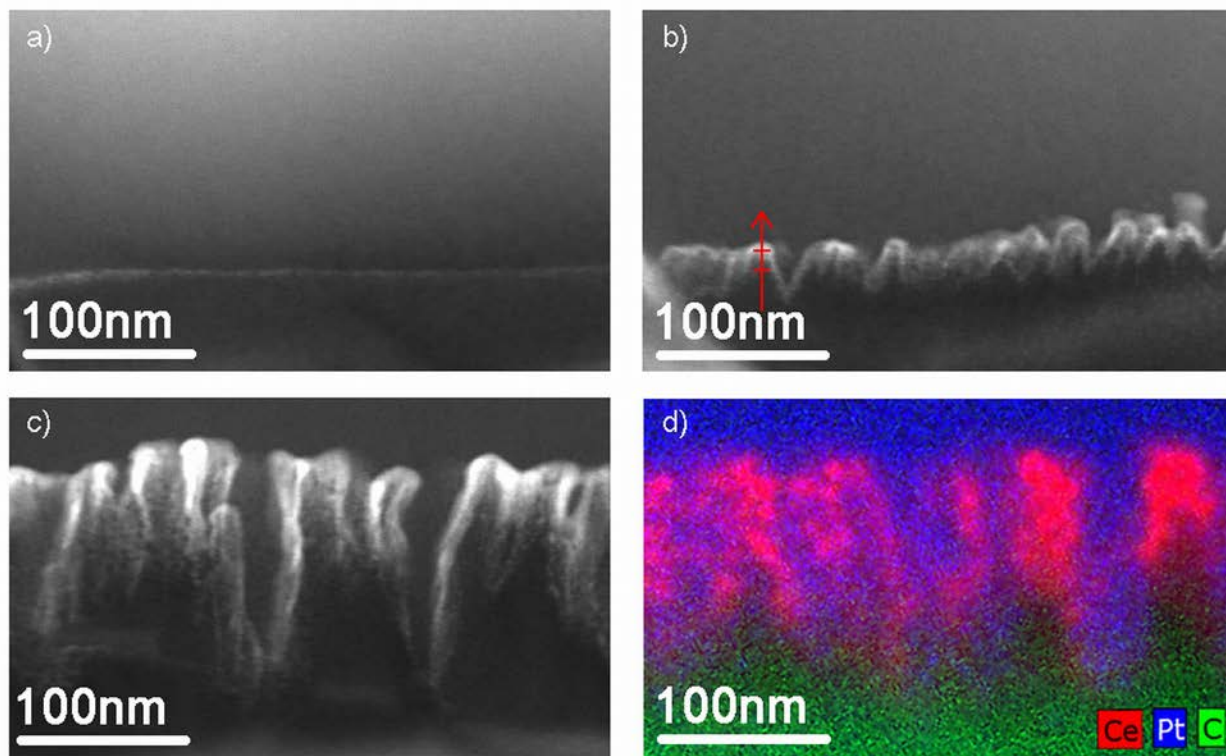

Fig. 2. The STEM cross-sectional images of the C-foil supported cerium oxide layers with nominal thicknesses a) 1 nm, b) 5 nm and c) 20 nm and d) the
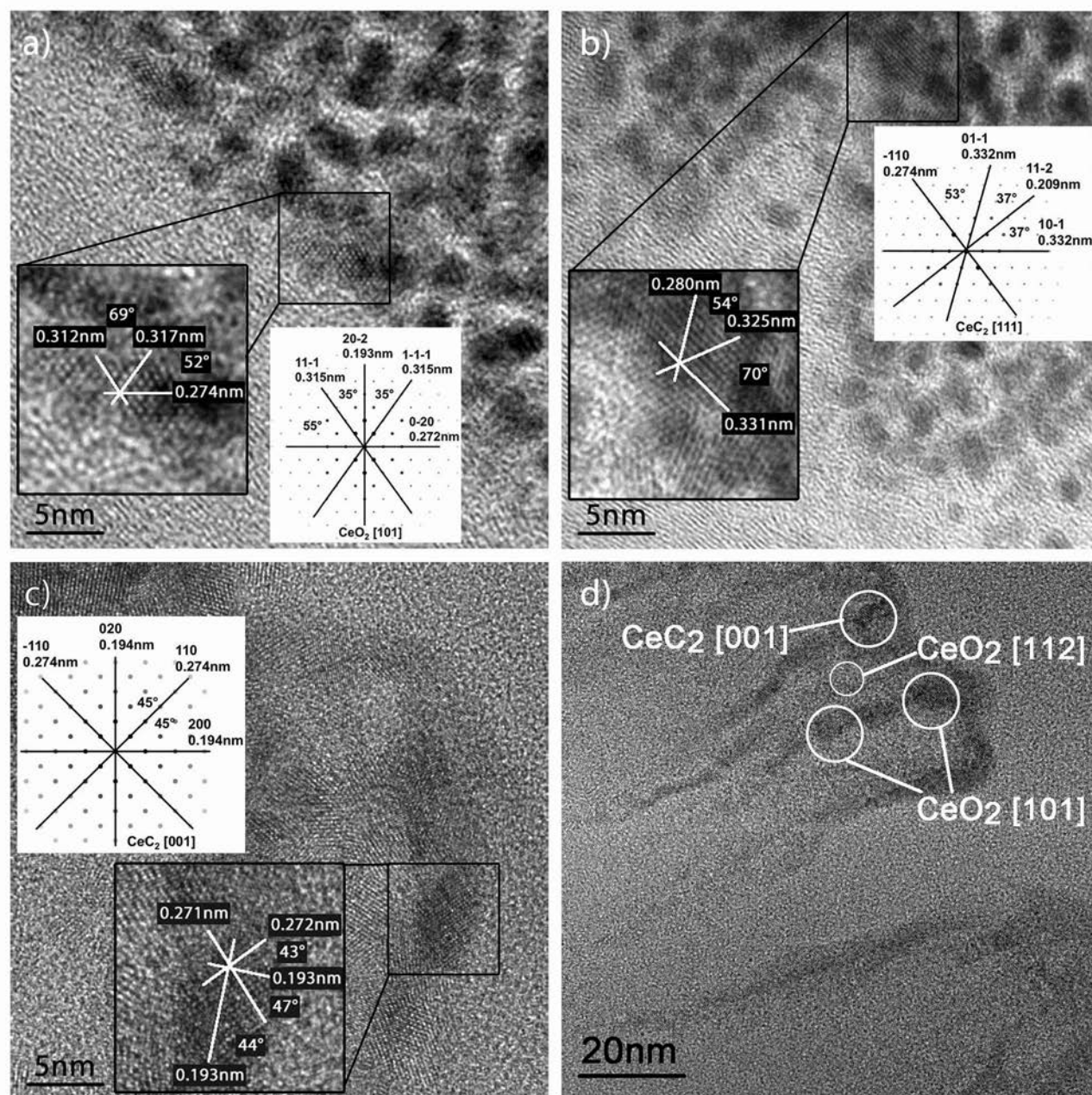10 EDX map of Ce (red), C (green) and Pt (blue) elements on the layer c). The hilly-like structure of carbon is created with increasing time of CeO$_2$ deposition.

Fig. 3. HRTEM micrographs of nanocrystals identified in the cerium oxide layers of different nominal thickness deposited on the C-foil surface: a) CeO_2 [101] (1 nm thick layer), b) CeC_2 [111] (5 nm thick layer), c) CeC_2 [001] (20 nm thick layer), and d) localization of some nanocrystals for CeO_2 (20 nm)/C-foil. For all images, the C-foil substrate is localized in left bottom areas.
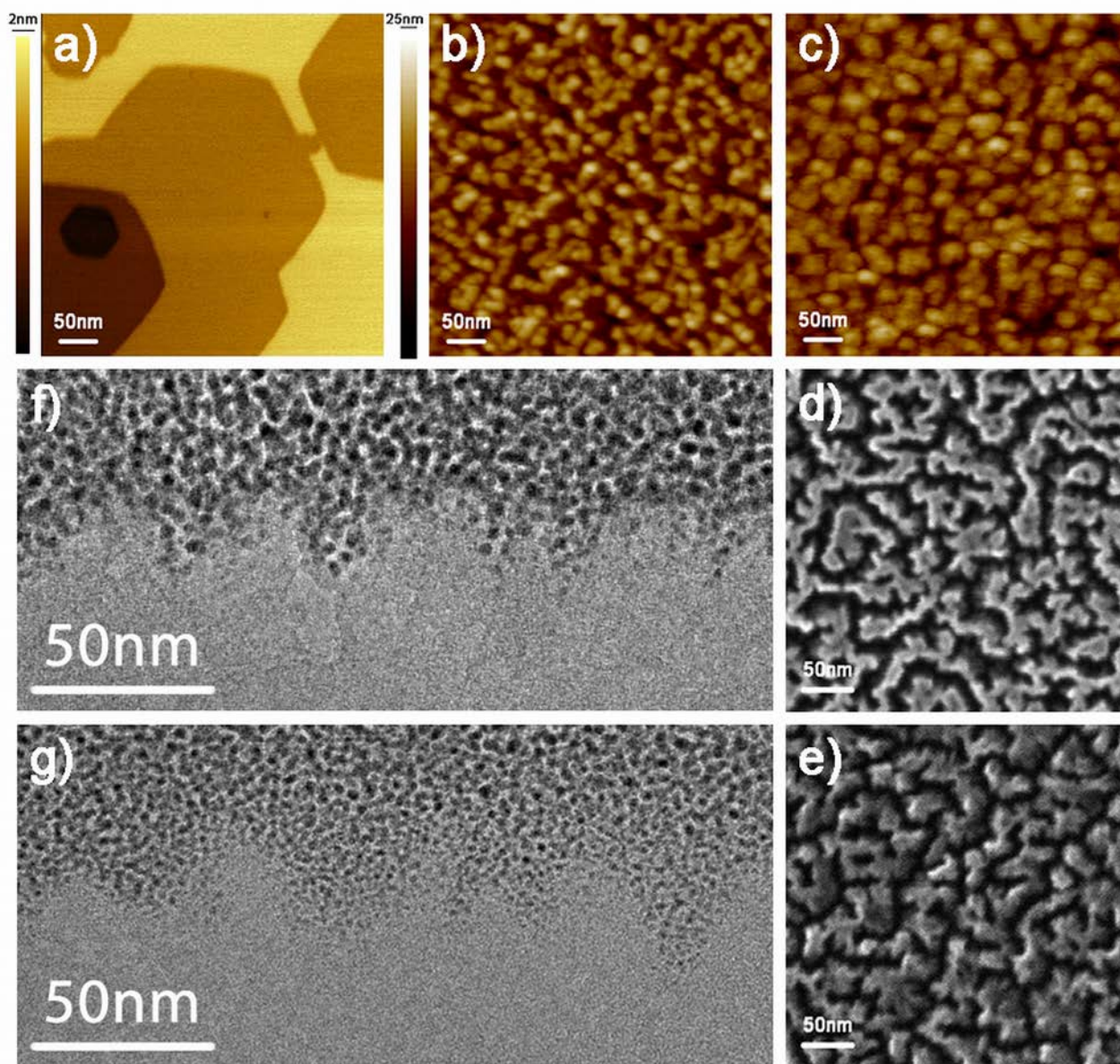
5

Fig. 4. Illustration of the key role of the carbon substrate in the formation of nanoporous catalyst layer. a) The high resolution AFM image of pure C-foil. The images of the surface of CeO_x (5 nm)/C-foil sample before and after removing the layer in H_2SO_4 acid obtained by AFM b) and c), by SEM d) and e) and by TEM f) and g), respectively.
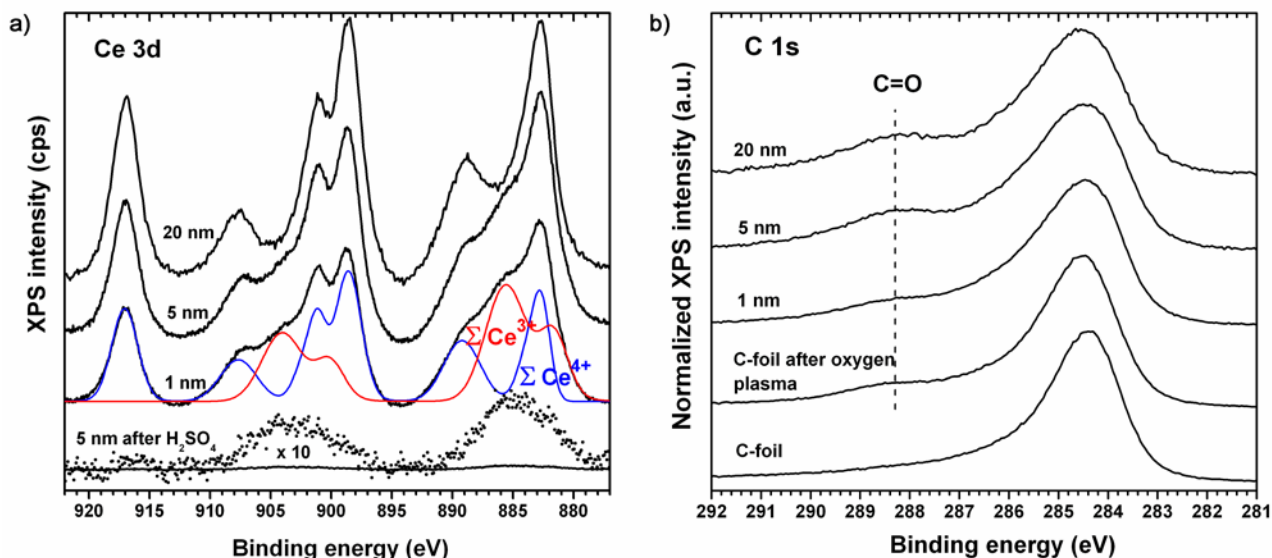
5

Fig. 5. XPS Ce 3d core level spectra of 1 nm, 5 nm and 20 nm of cerium oxide deposited on the C-foil and the spectra after removing the cerium oxide layer of 5 nm nominal thickness in H_2SO_4 acid (bottom curves). Red and blue lines represent the decomposition of the Ce 3d spectrum to sums of Ce^{4+} and Ce^{3+} doublets for 1 nm thick layer of CeO_x/C-foil a). XPS C 1s core level spectra of pure and oxygen plasma treated graphite foil and the spectra acquired
5 on the C-foil covered with cerium oxide of 1 nm, 5 nm and 20 nm nominal thicknesses b).
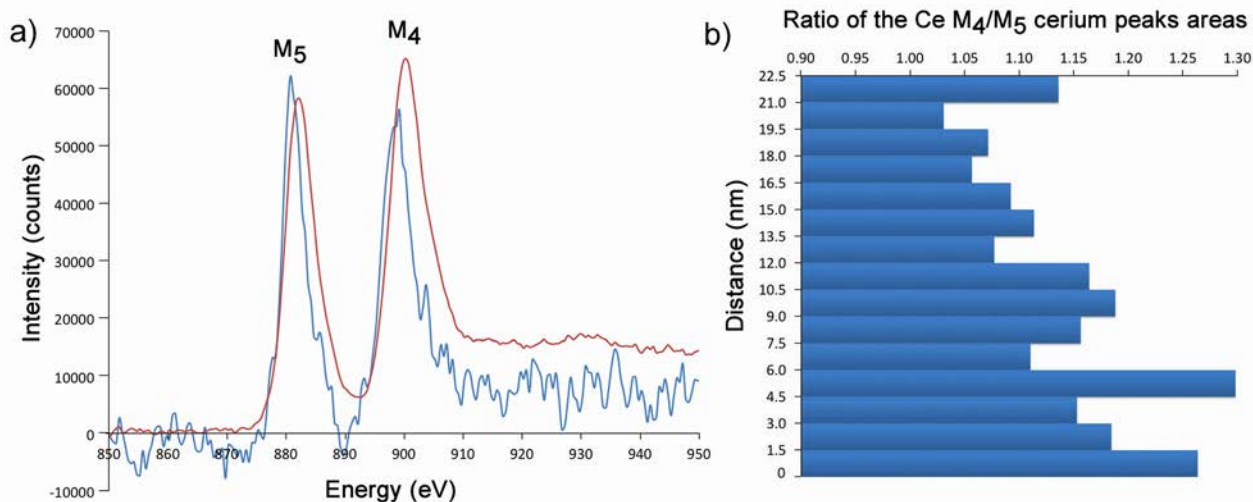

Fig. 6. EELS spectra of the Ce $M_{4,5}$ edges near the C-foil–CeO_x interface (red curve) and near the layer surface (blue one) on the CeO_x (5 nm)/C-foil sample a), plot of the A_{M5}/A_{M4} ratio calculated for each EELS spectrum of the linescan in the direction from C-foil-CeO_x interface to the layer surface
10 (marked by red arrow in Fig. 2b) b).

Fig. 7. Schematic layout of cerium ions in thicker layers of cerium oxide deposited by magnetron sputtering on the C-foil.

15